

MORPHOLOGICAL EVOLUTION OF A THREE-DIMENSIONAL CORONAL MASS EJECTION CLOUD RECONSTRUCTED FROM THREE VIEWPOINTS

L. FENG^{1,2}, B. INHESTER², Y. WEI², W. Q. GAN¹, T. L. ZHANG³, AND M. Y. WANG⁴

¹ Key Laboratory of Dark Matter and Space Astronomy, Purple Mountain Observatory, Chinese Academy of Sciences, 210008 Nanjing, China; lfeng@pmo.ac.cn

² Max-Planck-Institut für Sonnensystemforschung, Max-Planck-Str.2, 37191 Katlenburg-Lindau, Germany

³ Space Research Institute, Austrian Academy of Sciences, 8042 Graz, Austria

⁴ Shanghai Astronomical Observatory, Chinese Academy of Sciences, 200030 Shanghai, China

Received 2011 December 26; accepted 2012 March 14; published 2012 April 30

ABSTRACT

The propagation properties of coronal mass ejections (CMEs) are crucial to predict its geomagnetic effect. A newly developed three-dimensional (3D) mask fitting reconstruction method using coronagraph images from three viewpoints has been described and applied to the CME ejected on 2010 August 7. The CME's 3D localization, real shape, and morphological evolution are presented. Due to its interaction with the ambient solar wind, the morphology of this CME changed significantly in the early phase of evolution. Two hours after its initiation, it was expanding almost self-similarly. The CME's 3D localization is quite helpful to link remote sensing observations to in situ measurements. The investigated CME was propagating to Venus with its flank just touching *STEREO B*. Its corresponding interplanetary CME in the interplanetary space shows a possible signature of a magnetic cloud with a preceding shock in *Venus Express (VEX)* observations, while from *STEREO B* only a shock is observed. We have calculated three principal axes for the reconstructed 3D CME cloud. The orientation of the major axis is, in general, consistent with the orientation of a filament (polarity inversion line) observed by *SDO/AIA* and *SDO/HMI*. The flux rope axis derived by the Minimal Variance Analysis from *VEX* indicates a radial-directed axis orientation. It might be that locally only the leg of the flux rope passed through *VEX*. The height and speed profiles from the Sun to Venus are obtained. We find that the CME speed possibly had been adjusted to the speed of the ambient solar wind flow after leaving the COR2 field of view and before arriving at Venus. A southward deflection of the CME from the source region is found from the trajectory of the CME geometric center. We attribute it to the influence of the coronal hole where the fast solar wind emanated from.

Key words: Sun: corona – Sun: coronal mass ejections (CMEs)

Online-only material: animation, color figures

1. INTRODUCTION

Coronal mass ejections (CMEs) are huge explosions of magnetized plasma from the Sun. Their interplanetary counterparts, interplanetary coronal mass ejections (ICMEs), are considered to be the main driver of geomagnetic storms (Gonzalez et al. 1994). The major scientific objective of the *Solar Terrestrial Relations Observatory (STEREO)* mission (Kaiser et al. 2008) launched in 2006 October is to better understand the initiation and propagation of CMEs. A big advantage of the *STEREO* twin spacecraft is that they allow a simultaneous observation of a CME from two different perspectives. Quite a number of papers have been dedicated to the three-dimensional (3D) reconstructions of CMEs based on the coronagraph observations of the *STEREO* spacecraft.

Different reconstruction methods of coronagraph observations have been used in the past. Among them are forward modeling, triangulation method, polarization ratio method. A review on these methods can be found in, e.g., Mierla et al. (2010). Antunes et al. (2009) used a combination of forward and inverse method to estimate the CME mass distribution.

In this paper, we are aiming to obtain the 3D morphology of a CME by using the coronagraph observations from three viewpoints. Unlike forward modeling where a restricted family of geometrical CME shapes is assumed beforehand, our method allows any a priori shape of a CME. For tie-point approaches, the identification of corresponding structures from different views is required but is often difficult to achieve. The method described in the current work does not have this problem. The

polarization ratio method utilizes the polarizing properties of Thomson scattering. In principle, only one view is required. However, the information returned is only a depth surface representative of the scattering centers in the CME cloud along the line of sight. No information about the depth distribution can be retrieved. Moreover, the resulting plane bears the ambiguity of two symmetric solutions with respect to the plane of sky. The combination of forward and inverse methods of Antunes et al. (2009) also uses a forward modeling step essentially based on family of flux rope CME models. In a second step, the flux rope 3D volume is then used as the support for an inverse estimation of the density distribution of the CME. The latter step, however, is heavily under constrained and multiple solutions are possible.

Along with the very large variety of coronagraph reconstruction techniques, 3D geometric reconstructions using heliospheric imagers have also been developed by some authors, where a CME was treated as a complete volume rather than a point source. For example, Lugaz et al. (2009) used a 3D magnetohydrodynamic code to disentangle observational from physical effects. By comparing the simulation with the observations from coronagraph and heliospheric images, the 3D nature of two successive CMEs and their evolution in the inner heliosphere were studied. Tappin & Howard (2009) compared their model of interplanetary disturbances with heliospheric image data from the Solar Mass Ejection Imager. By identifying the simulated ICME that best matched the observations, they obtained the parameters that can describe ICME's 3D leading-edge structure, orientation, and kinematics.

The CME localization and morphology in 3D yield information about the CME's orientation, propagation direction, angular width in longitude, latitude, etc. and help to make reliable predictions about the arrival time of a CME at Earth or other planets. Reversely, in situ observations can be combined with near-Sun 3D reconstructions to constrain the CME model a posteriori. Such investigations aimed to study CME propagation properties in the interplanetary space have been performed by some authors, e.g., Möstl et al. (2009), Byrne et al. (2010), Liu et al. (2010a, 2010b), and Rodriguez et al. (2011). Rouillard et al. (2009) investigated a CME observed between the Sun and Venus using *STEREO*, *Venus Express* (*VEX*), and *MESSENGER* data. They compared the (I)CME orientation obtained by white light analysis with the in situ flux rope axis by *MESSENGER* and *VEX*. The CME orientation in the *STEREO*/COR2 field of view (FOV) was derived by a fit of the graduated cylindrical shell (GCS) model (Thernisien et al. 2006, 2009; Thernisien 2011). Due to the limited separation angle at the time of these observations, the GCS flux rope was only fitted to COR2 A. Early work before the *STEREO* era devoted to the comparison of the orientation of the source region neutral line, the CME cloud shape in coronagraph images and the flux rope axis orientation from in situ measurements have been made by Yurchyshyn et al. (2001), Cremades & Bothmer (2004), and Yurchyshyn (2008).

In this paper, we propose a new method for the reconstruction of the CME cloud based on the back projection of the observed CME periphery in multiple coronagraph images without any restriction by a predefined class of CME shapes. From the superposition of these back projections, we obtain a 3D volume which must contain the CME cloud entirely. Reversely, the real CME cloud also must fill this 3D volume in the sense that the cloud has to touch each wall of the 3D volume somewhere. Based on these principles, we propose a scheme to obtain an approximation to the real 3D CME cloud shape. Since the problem of 3D reconstruction from 2D images is notoriously under constrained, we have designed our scheme so as to incorporate images from as many different view directions as possible. In the application presented here, coronagraph data from the three spacecraft were used.

The paper is organized as follows. In Section 2, the coronagraph observations from three vantage points, *STEREO A*, *STEREO B*, and *Solar and Heliospheric Observatory* (*SOHO*), are described. Details of our reconstruction method are presented in Section 3. In Section 4, we use the 3D morphology obtained from our reconstruction to interpret in situ magnetic field and plasma parameters observed during the passage of the CME near Venus, Earth, and two *STEREO* spacecraft. The data we consider were obtained by the magnetometers (MAG) on board *VEX* orbiting Venus, *Advanced Composition Explorer* (*ACE*) orbiting Earth, and from the In-situ Measurements of Particles and CME Transients (IMPACT) and The Plasma and Suprathermal Ion Composition (PLASTIC) telescopes on board *STEREO*. From a series of 3D reconstructions with time, we are able to follow the CME morphological evolution. The height, speed evolution from the Sun to Venus are also discussed. The orientation of the filament in the source region, the orientation of the CME major principal axes and the flux rope axis direction derived from *VEX*/MAG data are compared.

2. OBSERVATIONS AND DATA REDUCTION

The CME we have investigated was observed on 2010 August 7 from three perspectives by the white light coronagraphs Large

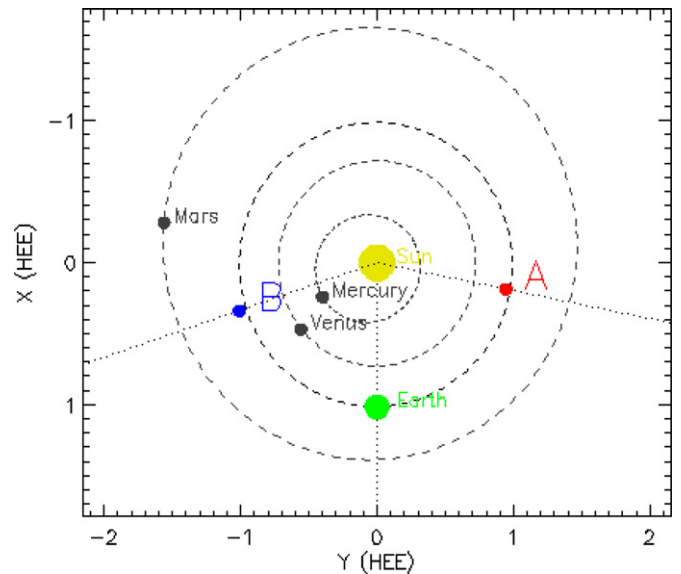


Figure 1. Relative positions of the two *STEREO* spacecraft, planets, and their orbits in the inner solar system in the frame of the HEE coordinate system. (A color version of this figure is available in the online journal.)

Angle Spectroscopic Coronagraph (LASCO; Brueckner et al. 1995) C2 and C3 on board *SOHO* (Domingo et al. 1995), and COR1 and COR2 in the Sun Earth Connection Coronal and Heliospheric Investigation (SECCHI; Howard et al. 2008) instrument suite on board *STEREO*. LASCO C2 has an FOV from 2 to 6 R_{\odot} , C3 from 3.7 to 30 R_{\odot} . COR1 reaches a lower altitude with its FOV from 1.4 to 4 R_{\odot} , COR2 from 2.5 to 15 R_{\odot} . On August 7, two *STEREO* spacecraft were separated by around 150 deg. The spatial positions of *STEREO A* and *B*, the planets, and their orbits in the inner solar system are presented in Figure 1 in the Heliocentric Earth Ecliptic (HEE) coordinate system. Venus was located between *STEREO B* and the Earth. The magnetometer on board *VEX* (Zhang et al. 2006) will be utilized to verify the CME propagation direction and to determine the CME arrival time at Venus.

In Figure 2 we present the time series of coronagraph images of the CME event for the three viewpoints employed. All images were processed by standard Solarsoft routines `secchi_prep` and `lasco_prep`. COR1 and COR2 images from *STEREO A* are shown in the first row, COR images from *STEREO B* are in the second row, and the C2 and C3 images from LASCO are presented in the last row. In each panel, the operated instrument and observational time are marked at the bottom. The occulter of the coronagraph is indicated as a black mask. As a size reference, we also plot the solar limb as a white circle onto each panel. Two different background subtraction methods have been applied here to make the CME leading edge and its related shock more prominent. For COR data, the respective pre-CME images were subtracted. For LASCO-C2, a 12 hr minimum image was created by taking the minimum brightness of each pixel during the 12 hr centered around the CME's first appearance. The dark area inside the CME in COR1 and COR2 indicates the position of a pre-existing helmet streamer which stayed more or less quasi-stationary during the CME evolution. The first appearance of the CME in COR1 A was at 18:15, in COR1 B at 18:25 UT, and in C2 at 18:36 UT.

For this particular CME, we identified shock signatures in the white-light observations. They appeared as a smooth front which outlined the CME's outmost envelope and was associated,

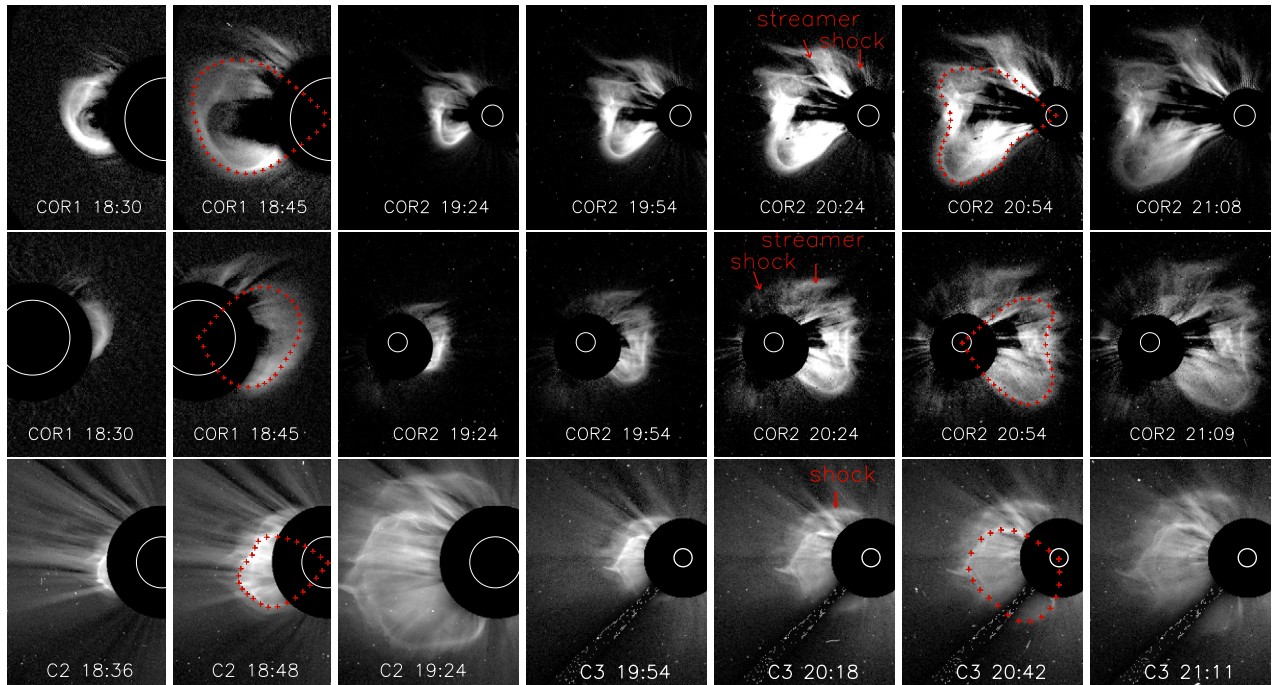


Figure 2. Selected coronagraph observations from three viewpoints. The top row shows COR1 and COR2 images from *STEREO A*, the middle row shows the COR1 and COR2 images from *STEREO B*, and the bottom row shows the LASCO C2 and C3 images from *SOHO*. The white circle in each panel indicates the limb of the solar disk and the dark round area is caused by the coronagraph occulter. For COR data, the respective pre-CME images are subtracted, while for LASCO data, a 12 hr minimum image is created and subtracted for C2 and C3. The small red plus signs mark the positions of CME peripheries.

(A color version of this figure is available in the online journal.)

spatially and temporally, with streamer deflections (Ontiveros & Vourlidas 2009). They are marked in column 5 in Figure 2 with two deflected streamers accompanying closely. At lower altitudes as in column 2, the shock looked like a diffusive area enclosing the CME cloud (Gopalswamy & Yashiro 2011; Gopalswamy et al. 2012). It is best seen in the C2 image of column 2 where the CME periphery is indicated by plus signs. The presence of a shock for this CME event is confirmed by the type II radio burst at a height of about $1.36 R_{\odot}$ (N. Gopalswamy 2011, private communication).

The shock signature can presumably be linked to the coronal EIT waves down to the FOV of EUVI (Wuelser et al. 2004) on board *STEREO* and AIA (Lemen et al. 2012) on board *SDO* (*Solar Dynamics Observatory*), which are 1.7 and 1.3 solar radii, respectively. In panels (a)–(c) of Figure 3, we present the dimming and the wave front in the running difference images observed by EUVI B, AIA, and EUVI A. An animation of the high-cadence AIA observations is available in the online journal where the coronal wave signature can be seen more prominently. The wave signatures observed above the limb were well connected to the wave signatures observed against the solar disk. EUVI A provided a better view of the wave dome. Inside the dome, the erupted prominence was visible in panel (f). The prominence in 30.4 nm is colored in red, while the wave front is colored in light blue. When the CME entered the COR 1 FOV (panel (e)), the CME periphery and shock front are delineated by plus signs and asterisk signs, respectively. In the same panel, the CME associated streamer belt is also shown. Details of the shock/EIT wave analysis is beyond the scope of this paper and will be pursued in a separate paper. Similar wave behavior and related quantitative analyses can be found in, e.g., Veronig et al. (2010).

The subtraction of the pre-CME image somehow removed part of the internal structure of the CME. To make the internal

structures visible, for COR 1 images we applied the 12 hr minimum image as well. The resulting images are shown in panel (d) of Figure 3. The CME periphery we used for 3D reconstruction is indicated by black asterisk signs. We tried to exclude as well the sheath between the shock front and the CME which manifested as a diffusive region there. Red plus signs represent the outer boundary of the CME cavity and the area inside green signs indicates the core region. For this CME, we found that its internal structure is a little bit complicated. In the cavity, it seems that a bright line feature appeared. If we regard the CME flux rope as the cavity and the prominence attached below (Chen 1996), the area inside the red signs is mainly the CME flux rope and possibly some material following it. Except for the unknown part hidden behind the occulter, we found that the CME flux rope occupied most of the area surrounded by the black signs, which we used for the 3D reconstructions.

In order to locate the CME source region, we have checked EUV images at various wavelengths taken by the EUVI instrument on board *STEREO* and by the AIA telescope on board the *SDO* spacecraft. At the time of the CME launch, an M1.0 class flare occurred in active region AR 11093 located at N12E31 as viewed from Earth on August 7. According to *GOES* light curves, the flare started around 17:55 and peaked at 18:24. Magnetograms from HMI (Helioseismic and Magnetic Imager; Scherrer et al. 2012) were used to determine the orientation of the magnetic polarity inversion line in the CME source region.

3. 3D RECONSTRUCTION METHOD

3.1. 3D Reconstruction and Smoothing

In the traditional stereoscopic technique, two corresponding points from an image pair are back projected along the respective line of sight to obtain their 3D coordinates (Inhester 2006; Feng et al. 2007a, 2009; Liewer et al. 2009, 2011). de Koning et al.

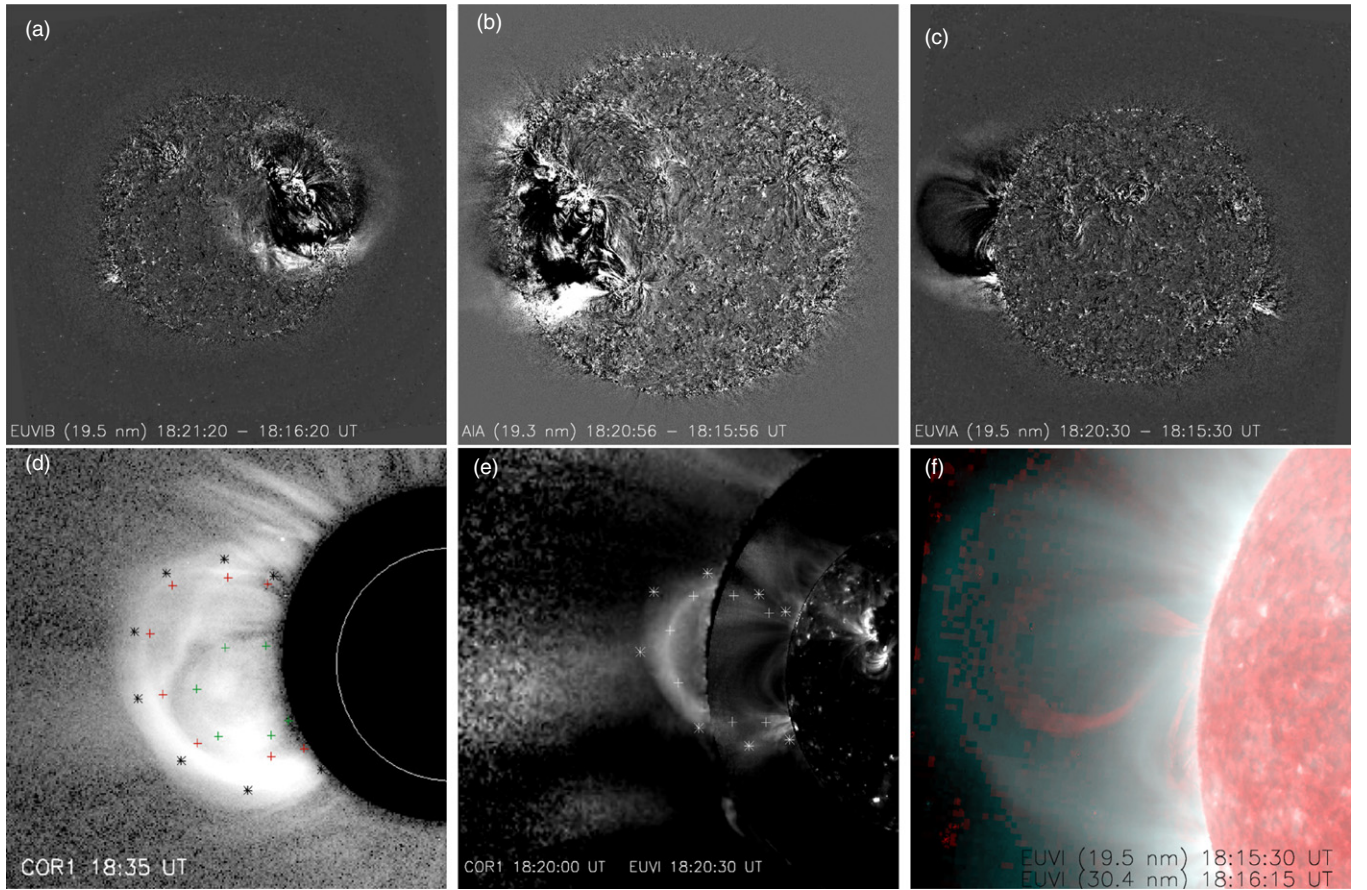


Figure 3. Panels (a)–(c) are the running difference images of the dimming region and the coronal EIT waves observed from EUVI B, AIA, and EUVI A. In panel (f), the red color channel represents the erupted prominence at 18:16 UT in 30.4 nm and the light blue channel represents the plasma emission at 18:15 UT in 19.5 nm, where we can see the dome-shape wave overlying the prominence. In panel (e), the CME periphery and its preceding shock front are indicated in plus signs and asterisk signs, respectively. In panel (d), the internal structure of the CME is presented. The black asterisk, red, and green plus signs indicate the CME leading edge, cavity outer boundary, and core region, respectively.

(An animation and color version of this figure are available in the online journal.)

(2009) geometrically reconstructed the CME location plane by plane from two viewpoints. The authors selected two points on the CME boundary in each image and back-projected to the Sun totally four points which lie in the same plane. Their back-projections formed a quadrilateral in that specified plane where the CME is ideally localized. Later, de Koning & Pizzo (2011) included the geometric localization method into the polarimetric technique to remove the ambiguity inherent in this technique.

The idea of our reconstruction method employs the inverse approach of the traditional stereoscopic technique. In this newly developed method, we forward project a point in the 3D space onto each coronagraph image. If the three projections are all located inside the respective CME periphery observed in each image, this 3D point is considered as a point inside a 3D volume which must contain the 3D CME cloud entirely. On the other hand, for the CME surface to be consistent with the observed peripheries, it must be close enough to the boundary of the reconstructed 3D volume so that their projections onto the coronagraph images coincide.

As the first step, we identify the CME periphery in each coronagraph image. At the moment, it is done by tie-pointing the CME leading edge in each image. The tie-points are then interpolated by a parametric cubic spline to obtain a smooth periphery curve. Examples of periphery tie-points are shown in columns 2 and 6 of Figure 2. Since we do not know how the CME continues behind the occulter, we simply extrapolate the

ends of the periphery curve from the occulter edge radially to the Sun’s surface. The result of this step is saved as binary masks $M_i(x_{p,i}, y_{p,i})$ for each image $i = A, L, B$ taken by *STEREO* A, *LASCO*, and *STEREO* B, respectively. We set M_i to unity at image pixels $(x_{p,i}, y_{p,i})$ inside the periphery curve and to zero outside. Note that the *LASCO* images were not always recorded exactly simultaneously to those from *STEREO*. In these cases, the CME periphery curves from two neighboring frames in time from *LASCO* were interpolated to the time of the *STEREO* observations.

As the next step, we select a regular 3D mesh of the space around the Sun. In our method, the distance of grid points is chosen adaptively depending on the projected CME size in the images. Since we are considering a time evolution problem, all calculations in this work are performed in a Cartesian Carrington coordinate system. For each 3D grid point $\mathbf{r} = [x, y, z]$ we obtain its projection $\mathbf{r}_{p,i}$ onto image i by Feng et al. (2007b):

$$\mathbf{r}_{p,i} = A_i^T \mathbf{r} \quad (1)$$

where A_i is the matrix of the coordinate transform

$$A_i = \begin{bmatrix} -\sin L_i & -\cos L_i \sin B_i \\ \cos L_i & -\sin L_i \sin B_i \\ 0 & \cos B_i \end{bmatrix}$$

and L_i and B_i are the longitude and latitude of spacecraft i in the Carrington coordinate system. After projecting a 3D point

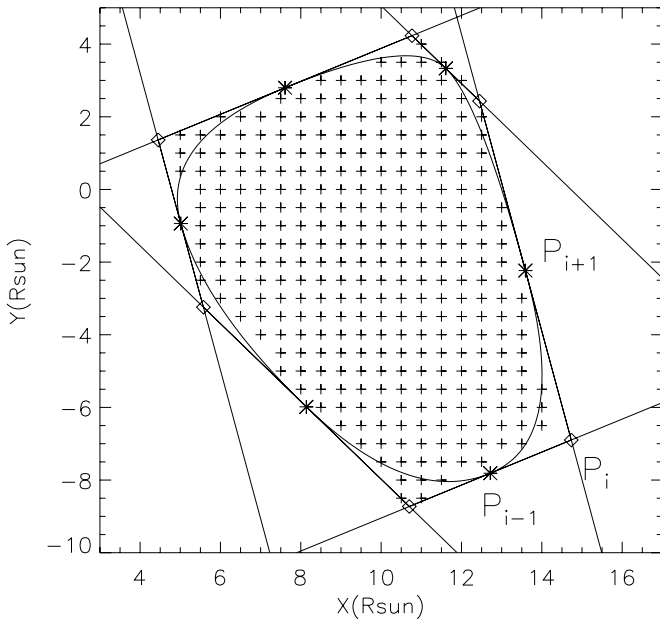


Figure 4. Smoothing of the CME cloud by quadratic Bézier curves in one horizontal plane parallel to the solar equatorial plane. The plus signs are the 3D CME points lying in this plane from the mask fitting method. Three pairs of parallel lines are the projections of line of sights from *STEREO A*, *STEREO B*, and *SOHO* onto this horizontal plane. Their intersections are shown by diamonds and the respective middle points are marked by asterisks. The Bézier curves are shown by a smoothed consecutive curve which is tangent to the projected line of sights.

\mathbf{r} onto all three coronagraph masks M_i , we set a 3D mask M_{3D} according to

$$M_{3D}(\mathbf{r}) = \begin{cases} 1 & \text{if } M_i(\mathbf{r}_{p,i}) = 1 \text{ for all } i = A, L, B \\ 0 & \text{if } M_i(\mathbf{r}_{p,i}) = 0 \text{ for one or more } i. \end{cases} \quad (2)$$

This process is repeated for all 3D points until the 3D mask M_{3D} is completely determined. This mask then defines the embedding 3D volume containing the CME cloud.

As an example of the reconstructed 3D mask we show a horizontal cut of M_{3D} which yields the polygon in Figure 4. The mask area is marked by plus signs at the respective grid points. The region defined by mask M_{3D} may include areas which do not belong to the true CME area but are still covered by the projections of the 2D image masks. Assuming the real CME surface is smooth, these areas are probably confined to the vicinity of the vertices of the polygon from M_{3D} . These vertices occur naturally where the boundaries of the back projected 2D masks intersect. From three images there are up to six vertices possible in every horizontal plane intersecting M_{3D} . In Figure 4, these vertices are marked as diamonds.

In a final step, we smooth the corners of M_{3D} . For each horizontal plane, we find the centers on the faces of the 3D mask between each neighboring pair of vertices. In Figure 4, these centers are marked as stars. For each vertex we then define a quadratic Bézier spline

$$\mathbf{B}_i(t) = (1-t)^2 \mathbf{P}_{i-1} + 2(1-t)t \mathbf{P}_i + t^2 \mathbf{P}_{i+1}, \quad t \in [0, 1] \quad (3)$$

from the three control nodes P_{i-1} , P_i , and P_{i+1} . The central P_i is the vertex position and $P_{i\pm 1}$ are located at the face centers to either side to the vertex. This choice of the spline curve ensures that the boundary formed by the combination of all spline curves is continuous and smooth as demonstrated by the

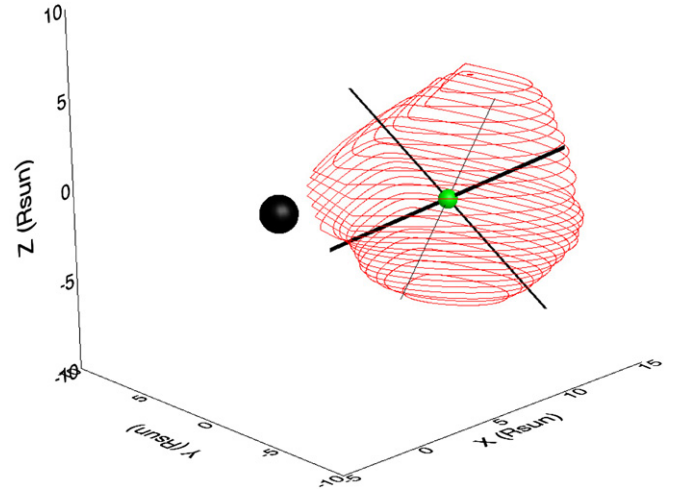


Figure 5. One example of 3D CME cloud and its three principal axes at 21:24 UT. The thickness of axis is proportional to the scale of eigenvalue. The green dot indicates the position of CME's geometric center.

(A color version of this figure is available in the online journal.)

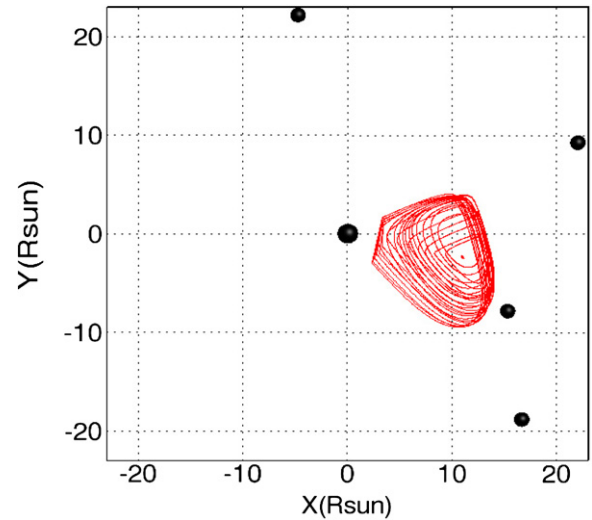


Figure 6. Perspective from a vantage point above the north pole of the Sun to show the localization of the CME relative to the Sun, Venus, Earth, and the two *STEREO* spacecraft at 21:24 UT. The Sun centers at (0,0). From top to bottom, the other four black spheres represent *STEREO A*, Earth, Venus, and *STEREO B*, respectively. Here their distances to the Sun have been scaled to 10% of their original values to just indicate their view directions.

(A color version of this figure is available in the online journal.)

example in Figure 4. This new boundary is finally adapted as the approximation to the CME shape in each horizontal plane.

Similar techniques were used in earlier papers. Byrne et al. (2010) fitted an ellipse to a quadrilateral which was derived from two viewpoints. However, our Bézier curve fitting has more flexibility and is readily adapted to include more than two view directions. Additional view directions provide more constraints to the 3D CME localization. However, we have to admit that as the control nodes on the face centers are selected somewhat arbitrarily, there is still some uncertainty about the real CME shape. From our procedure we obtain the surface with the least curvature compatible with the observations.

This fitting process described above is performed for each horizontal plane. In the end, a smoothed surface of the CME cloud is obtained. One example of such reconstruction is shown in Figure 5 and is represented by red curves. We have to mention

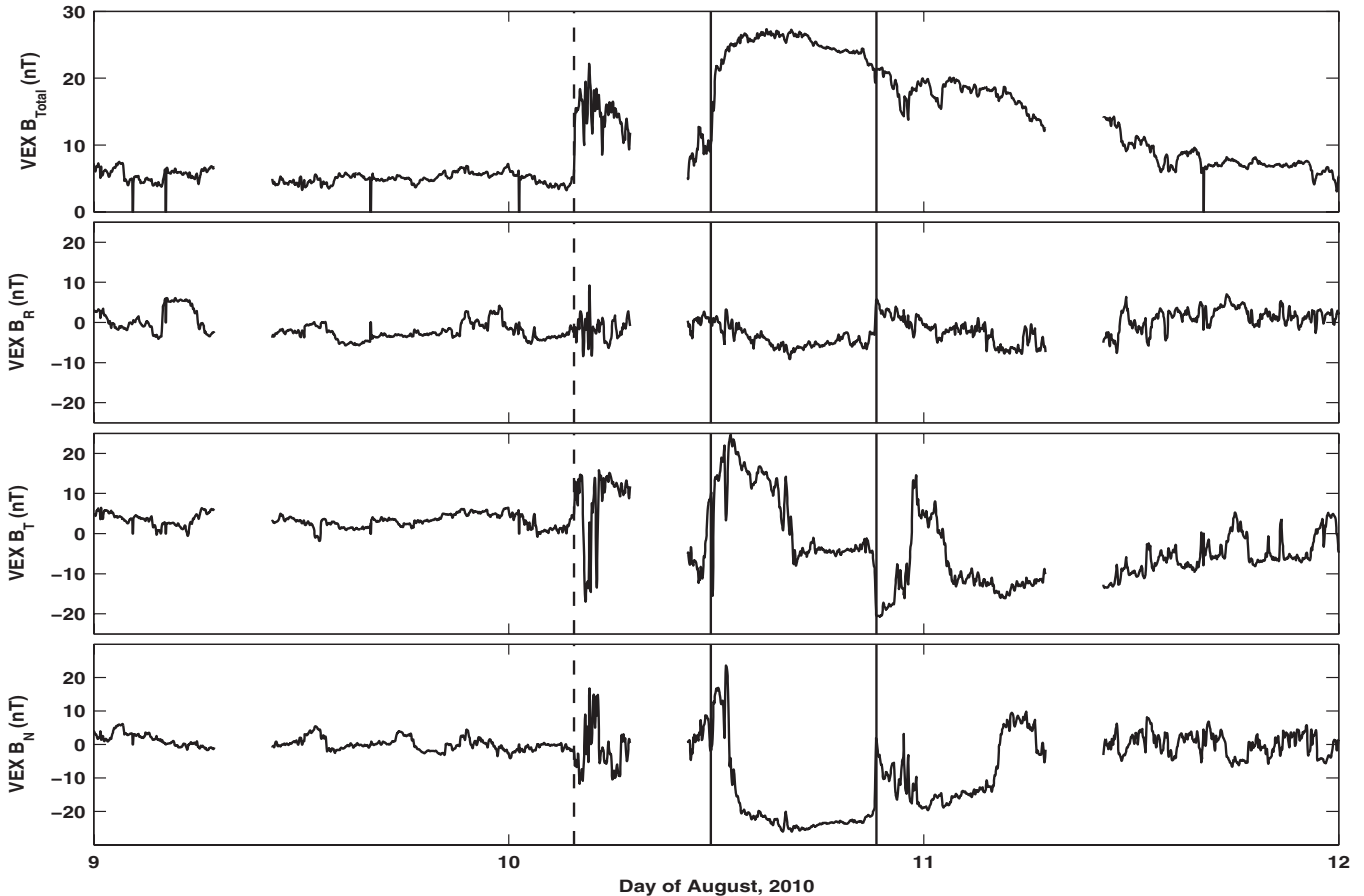


Figure 7. In situ measurements by MAG on board *VEX*. From top to bottom are the total magnetic strength, three magnetic field components in RTN coordinates. The signature of magnetic cloud is indicated by two vertical solid lines and the preceding shock is marked by the dashed line. *VEX* has an elliptical polar orbit with a 24 hr period, and stays in the Venusian magnetosheath and magnetosphere from 07:00 to 10:20 UT for each orbit. MAG continuously operates, but we block the data from 07:00 to 10:20 UT to focus on the solar wind structure.

that since the CME structure below the occulter is unknown, the CME cloud in the region inside the occulter radius from the Sun’s center is not plotted.

3.2. Calculation of the Geometric Center and Principal Axes

Since a determination of the density distribution in the CME cloud is a highly ill-posed problem and cannot be done reliably from only three view directions without further constraints, we take the CME shape as the basis for further analysis. We therefore neglect the internal structure of the CME in the analysis below and only characterize the shape of the cloud and its morphological evolution. Hence the center of the cloud may not be its center of gravity, but the geometric center which is still a significant quantity to characterize the position and motion of the CME cloud.

Natural characteristics of an amorphous volume are its geometric center (GC), and its three principal axes and their eigenvalues. The geometric center \mathbf{r}_{gc} of the CME cloud can be obtained from

$$\mathbf{r}_{\text{gc}} = \frac{\sum_{\mathbf{r}} V(\mathbf{r})\mathbf{r}}{\sum_{\mathbf{r}} V(\mathbf{r})}, \quad (4)$$

where $V(\mathbf{r})$ is unity inside the CME cloud and zero elsewhere. The principal axes and their eigenvalues are found from diagonalization of the matrix:

$$\frac{\sum_{\mathbf{r}} V(\mathbf{r})(\mathbf{r} - \mathbf{r}_{\text{gc}})(\mathbf{r} - \mathbf{r}_{\text{gc}})^T}{\sum_{\mathbf{r}} V(\mathbf{r})}. \quad (5)$$

These integrations are performed straightforwardly on the 3D grid chosen to generate the mask $M_{3\text{D}}$. Grid cells intersected by the boundary of $V(\mathbf{r})$ are weighted according to their overlap with $V(\mathbf{r})$.

In Figure 5, we plot the directions of three eigenvectors calculated from the matrix diagonalization for the CME cloud at 21:24. The thickness of the three principal axes is proportional to the magnitude of the eigenvalues. All three eigenvectors are centered at the CME’s geometric center. We name them minor, intermediate, and major axes, respectively, according to the order of their eigenvalues.

4. RESULTS

Based on the reconstructed 3D surface of the CME cloud, further analyses can be made. A straight forward application is to identify the longitude and latitude of the CME cloud and its spatial extension in 3D. This information can assist us in interpreting in situ measurements. From a time series of the 3D cloud, the CME’s morphological evolution and propagation properties can be derived.

4.1. Interpretation of the In Situ Data

From the space weather point of view, the longitude and latitude position, the angular width of the CME cloud are very crucial to determine whether or not a CME can interact with a planet’s magnetosphere or a spacecraft.

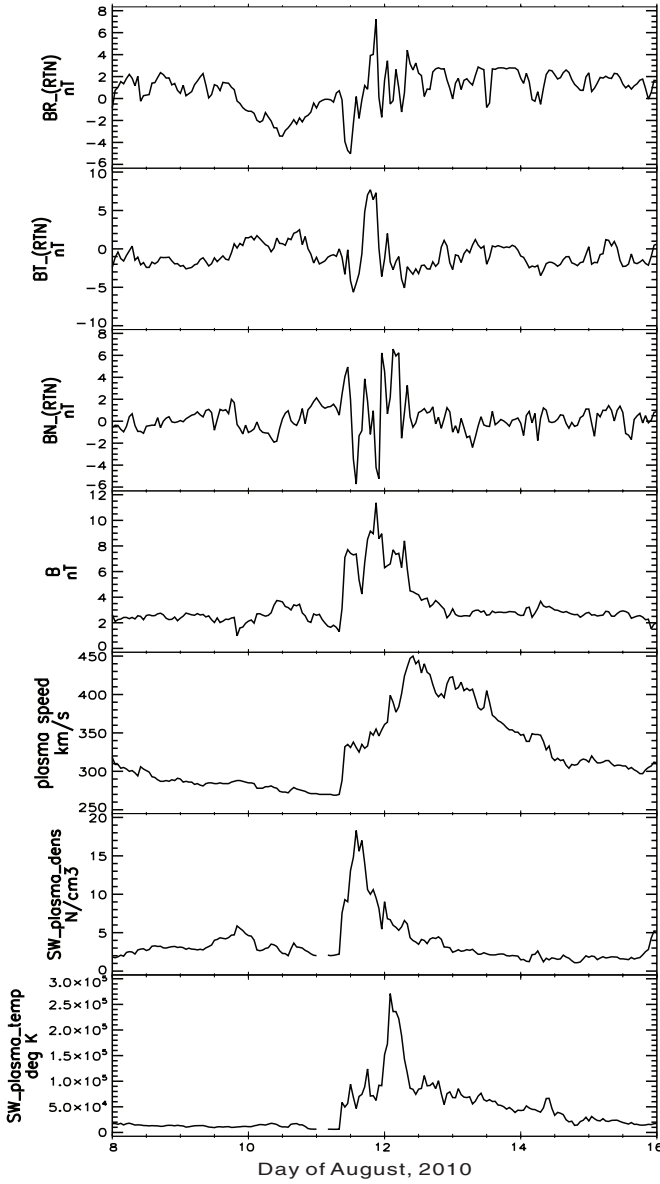


Figure 8. IMPACT and PLASTIC data with a temporal resolution of one hour from *STEREO B*. From top to bottom are the magnetic field components in RTN coordinates and its total strength, the proton density, bulk speed, and proton temperature.

Figure 6 provides a view from a vantage point above the solar north pole in which the localization of CME relative to the Sun, Venus, and two *STEREO* spacecraft is indicated. The CME that initiated on August 7 was propagating closely toward Venus. In Figure 7, we present the magnetic field measurement by the Magnetometer on board *VEX/MAG* from August 9 to 12. From top to bottom, we plot the total magnetic strength and three magnetic field components in the Radial–Tangential–Normal (RTN) coordinate frame. Here, vector R is the unit vector from the Sun to the spacecraft, T is the unit vector in the direction of the cross product of R and solar rotational axis, and N completes the right-handed triad. *VEX* has an elliptical polar orbit with a 24 hr period, and stays in the Venusian magnetosheath and magnetosphere from 07:00 to 10:20 UT for each orbit. *MAG* continuously operates, but we block the data from 07:00 to 10:20 UT to focus on the solar wind structure.

On August 10, from about 04:00 UT *MAG* we detected a sudden discontinuous increase in the magnetic field strength and

Table 1
Eigenvalue Analysis at Different Time Instances

Time	2D Uncertainty (arcsec)	Major/Minor	Intermediate/Minor
18:48	85.8 ± 22.15	2.43 ± 0.111	1.68 ± 0.066
19:24	133.9 ± 16.91	2.02 ± 0.087	1.71 ± 0.096
19:54	115.1 ± 18.34	2.35 ± 0.104	1.70 ± 0.095
20:08	116.7 ± 16.54	2.11 ± 0.075	1.53 ± 0.057
20:24	112.5 ± 17.47	2.13 ± 0.073	1.52 ± 0.048
20:39	125.0 ± 25.05	2.01 ± 0.086	1.52 ± 0.071
21:08	155.8 ± 21.27	1.90 ± 0.109	1.50 ± 0.052
21:24	143.3 ± 16.12	1.95 ± 0.054	1.56 ± 0.075

Notes. The first column shows the average distance between the traced 2D CME peripheries and its standard deviation. The second column is the ratio of eigenvalues between the major and minor axes, and the third column is the ratio of eigenvalues between the intermediate and minor axes. The values after the plus–minus sign are the standard deviation of the ratios. The uncertainty is propagated from the uncertainty of the 2D coordinates.

abrupt changes in the field direction. It is likely to be the shock and sheath signature preceding an ICME. Further verification also requires a sudden increase in flow speed, density, and thermal speed. Unfortunately, plasma measurements by *VEX* was not available for the solar wind structure. The spacecraft enters the Venusian ionosphere when plasma measurements are made. From 11:00 UT on the same day, the magnetic field strength was enhanced and smooth rotations of the field were found. It implies the appearance of a magnetic cloud. Due to the lack of plasma measurements, a further proof of the lower proton temperature is not available in Figure 6.

The magnetic field and plasma measurements in Figure 8 taken from the IMPACT and PLASTIC particle spectrometers on board *STEREO B* only show the signature of a shock which appeared around 10:00 UT on August 11. From top to bottom, we plot the magnetic field in RTN coordinates and its total strength, the proton density, the bulk speed, and the proton temperature. We did not see any clear ICME at *STEREO B* following the shock. This observation can be explained by checking the CME localization relative to the line connecting the Sun and *STEREO B* in Figure 6. The flank of the reconstructed CME cloud just touches this connection line which is an evidence that the cloud did not pass *STEREO B*. However, since the shock has a larger spatial extension than the cloud, it was still observed at the spacecraft. The projected shape of the CME on the solar equatorial plane indicated that the CME was mainly directed towards *VEX* and *STEREO B*. Unfortunately, we do not have direct observations of the shock on the equatorial plane; we speculate that the in situ shock signature might be more prominent in the *VEX* and *STEREO B* observations. We did not see any signature of an ICME and/or a shock in the *ACE* data observed at L1 point.

4.2. Morphological Evolution of the 3D Cloud

By following the variation of the calculated eigenvalues and eigenvectors, we can deduce the CME’s morphological evolution. In Table 1, the ratio of the eigenvalues of the major to the minor axes and of the intermediate to the minor axes are listed. The related uncertainties are propagated from the 2D CME tracing uncertainties. In the first column, the average distance between the traced CME peripheries and its standard deviation are presented. Here the 2D uncertainty is derived by repeating the tracing process ten times. It can be seen that

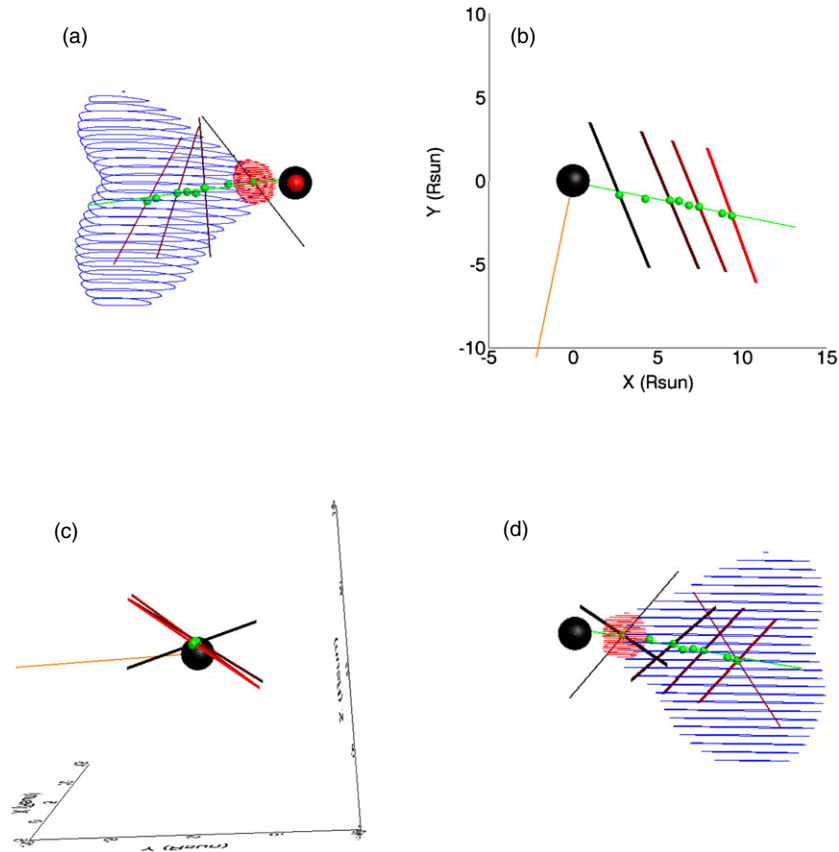


Figure 9. Orientation of the principal axis at the four time instances of 18:48, 19:54, 20:39, and 21:24 UT. The color of the principal axis varies from black to red. The green dots are the geometric center of the CME cloud at different times, and the green solid line is a linear fit in 3D and indicates the CME propagation direction. The orange solid line lies in the solar equatorial plane and perpendicular to the propagation. Panel (a) A view from *STEREO A* of the intermediate principal axes together with the projected 3D CME at 18:48 and 21:24 UT in red and blue, respectively. Panel (b) A view of the major principal axes from a vantage point above the north pole. Panel (c) A view of the major axes along the propagation direction. Panel (d) A view of the major axes along the line in orange and the corresponding projected 3D CME at 18:48 and 21:24 UT in red and blue, respectively.

(A color version of this figure is available in the online journal.)

the major morphological differences occurred during the first three time instances. After 20:08 UT, the shape appears to have remained stable. This trend can also be seen from the orientation of the principal axes in Figure 9.

We have to admit that our reconstruction is subject to another uncertainty. From the coronagraph observations we can only observe the part of CME outside of the occulter. This produces a larger uncertainty on the reconstructed CME shape in the early phase of propagation when a non-negligible part of CME was still below the occulter. Therefore, the orientation of the reconstructed CME cloud at the earliest time in Figure 9 might have relatively big error bars.

In panel (a) of Figure 9, the intermediate principal axis at four different time instances is shown from the viewpoint of *STEREO A*. The black sphere represents the Sun, the red sphere represents *STEREO A*. The green dots are the geometric center at different times. And the green line is the linear interpolation of these green dots indicating the CME propagation direction. The projected CME cloud at 18:48 UT and 21:24 UT is presented as well in red and blue in panel (a), respectively. We find that the orientation along which the CME is most extended as seen in COR A is more or less consistent with the intermediate axis, not with the major axis. It implies that for this CME, the most elongated direction in 3D is not lying in the projected COR A image plane.

The evolution of the intermediate axis shows big changes in orientation from 18:48 UT to 20:39 UT. This shape change is

also evident in COR A observations. In the early phase of the propagation, the northern part was moving ahead of the southern part. The reason is that the northern part of the filament related to this CME erupted first (Reddy et al. 2012). Later on, the southern part of the CME entered the fast solar wind region and was probably accelerated. The interaction of the CME with the fast and slow solar wind components likely produced a heart-like shape. The slow solar wind appears to originate from a region that is known as the streamer belt, which was around the solar equatorial plane as can be seen in panel (e) of Figure 3. Because the CME had a speed (see Section 4.4) greater than the slow solar wind, say typically about 400 km s^{-1} , it significantly decelerated near the streamer belt, whereas the part of CME in higher latitudes might even be accelerated, if the ambient fast solar wind had a higher speed. Varying conditions at different latitudes likely caused the distortion of the CME structure. It can also be seen in panel (a) that the propagation of the CME geometric center points more or less to the dip of the concave inward bulge of the CME shape which marks the position of the streamer belt.

Panel (b) shows the major axis projected onto the solar equatorial plane. The thin orange solid line is the direction perpendicular to the CME propagation. We find that the orientation of the major axis does not show much variation during the CME evolution. Interestingly, it is not perpendicular to the propagation direction. The asymmetry with respect to the propagation

direction probably reflects a west–east asymmetry of the filament eruption.

Panel (c) presents the evolution of the major axis as seen along the propagation direction. Again we find an almost constant orientation during the later phase of the CME evolution. Our analysis indicates a rotation of the major axis in the early stage from 18:48 UT to 19:54 UT. However, this rotation might also be due to the uncertainty of the CME shape at 18:48 UT introduced by the part of the CME still hidden behind the occulter. A comparison of the orientation of the CME with the related filament and in situ ICME will be discussed in Section 4.3.

The last panel in Figure 9 shows the intermediate and the major axes together with the projected CME cloud as seen from the perspective perpendicular to the CME propagation at 18:48 UT and 21:24 UT. The major axis at 19:54 UT and 20:39 UT from this perspective are plotted as well. It is clear that the shape has changed significantly from 18:48 UT to 21:24 UT. Again, the most obvious change is during the early phase of the evolution.

4.3. The Source Region and Orientation Comparison

Extrapolating the CME geometric center propagation direction backward to the solar surface, we arrive at a location very close to AR 11093. Considering the error bar of the 3D reconstructions especially at the early phase of the propagation, the active region may be regarded as the possible source region. The extrapolation of the geometric center is quite helpful for the identification of a CME’s source region, especially around the solar activity maximum when there are multiple active regions and more frequent activities.

Reddy et al. (2012) and Srivastava & Murawski (2012) made detailed analyses of AR 11093. They found that it was the rising of a filament that led to an M 1.0 class flare and the CME on 2010 August 7. Here we present some complementary investigations of the source region. In Figure 10 are AIA and HMI observations. The upper panel shows the EUV image at 304 Å right before the flare with HMI magnetogram contours overlotted. The lower panel shows the post-flare arcades observed at 171 Å by AIA well after the CME release.

From *GOES* observations we find that the flare started around 17:55 UT and peaked at 18:24 UT. The filament marked 1 in Figure 10, upper panel, rose before the flare, which is also indicated by the deviation of this filament from the magnetic polarity inversion line (PIL). As filament 1 is relatively high, the projected filament is, due to the projection effect, not lying along the PIL. However, filament 2 seems to be consistent with the PIL. Its disappearance is probably related to the heating by the flare.

The orientation of the PIL in the active region approximated by filament 2 can be compared with the orientation of the major principal axis calculated from the 3D CME cloud and the flux rope orientation deduced from the *VEX*/MAG data. We note that the orientation derived from the *VEX* data only involves the flux rope component in a CME, while the major axis of the reconstructed 3D CME is related to the leading edge, flux rope, and possibly some material following it. In Section 2 we found that the CME flux rope in the coronagraph image occupied most of the area which we used for the 3D reconstructions, the major axis is used as a first approximation of the orientation of the 3D CME flux rope.

The filament is curved as seen from Figure 10; we can only make a rough comparison. The general orientation of the filament lies in the direction from northeast to southwest

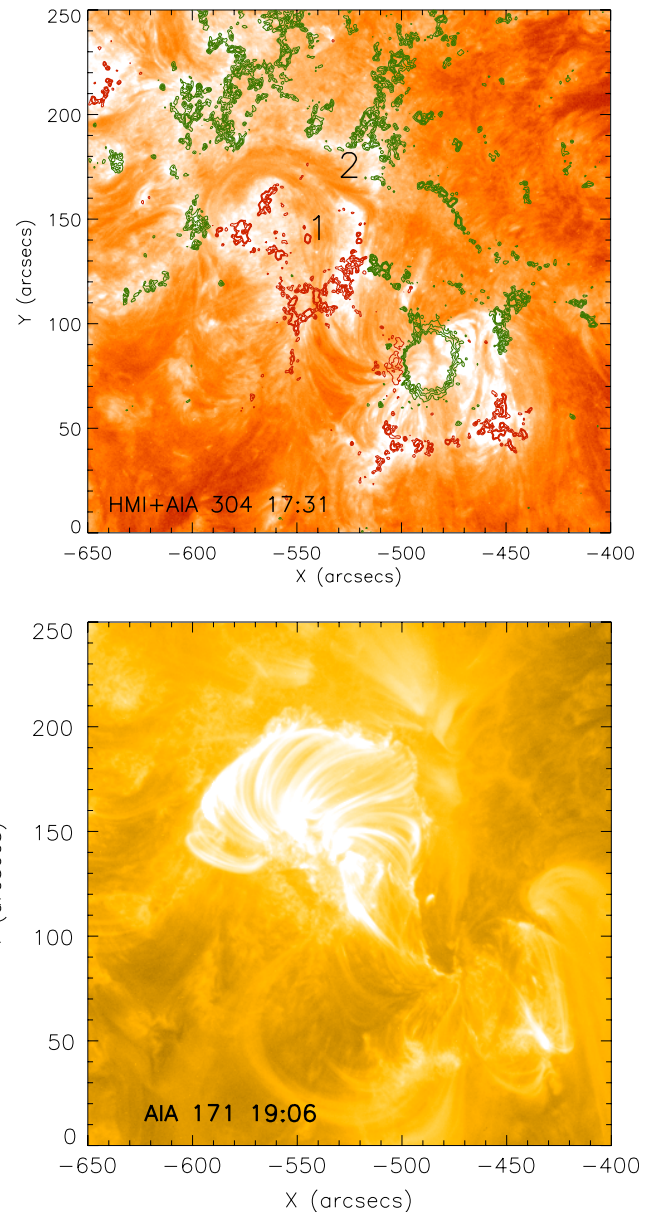


Figure 10. Upper: AR11093 at 17:31 UT before the flare occurrence. It is recorded by AIA 304 Å and HMI magnetogram. The background is the 304 Å image and the red and green contours are the positive and negative polarities in the HMI. Bottom: the post flare arcades observed at 171 Å by AIA.

(A color version of this figure is available in the online journal.)

which is consistent with the major axis indicated in panel (c) of Figure 9. The orientation of the flux rope observed by *VEX* was computed by the Minimal Variance Analysis (MVA) method. It has a direction of (0.96, 0.01, -0.29) in the RTN coordinate system, which means that the detected flux rope is mainly in the radial direction. Compared with the flux rope orientation in the remote-sensing data, there is a big difference. From the top view of the reconstructed 3D CME in Figure 6, it seems realistic that only the leg of the flux rope structure passed through *VEX*. In consequence, the orientation measured by MAG indicates a nearly radial direction. If a spacecraft traveled through different parts of the magnetic cloud, the flux rope orientation seen by the spacecraft may vary significantly. A diagram depicting the possible *VEX* spacecraft path in the magnetic flux rope is shown in Figure 11. However, if the spacecraft went through the flux

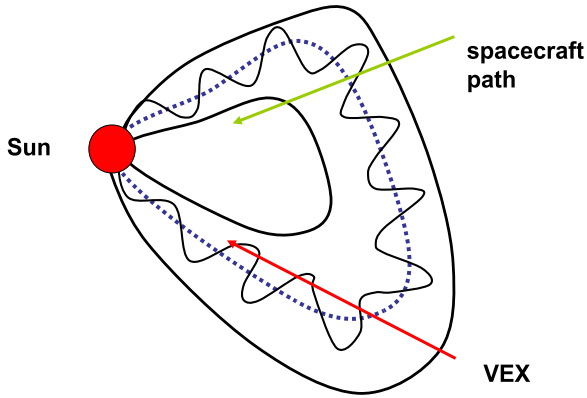


Figure 11. Schematic view of the magnetic flux rope with respect to the spacecraft position. The blue dotted line indicates the flux rope axis. The red line represents a possible path of *VEX* in the flux rope. The green line is an arbitrary path.

(A color version of this figure is available in the online journal.)

rope along the green path, we might arrive at a flux rope axis almost perpendicular to the green direction.

4.4. Propagation Direction, Height, and Speed Evolution

In Figure 12, the trajectory of the CME geometric center is plotted. The figure shows its distance from the Sun and its longitude and latitude. Near the Sun, the geometric center has an average speed near around 512 km s^{-1} . The averaged longitude and latitude in the Carrington coordinates are -12.8 and -6.18 deg, respectively. The CME was propagating roughly in the radial direction. However, the latitude decreases from the source region at around 12 deg in the northern hemisphere to -9 deg in the southern hemisphere at a distance of about 10 solar radii. Similar deflections of a CME have been reported by Cremades & Bothmer (2004) and other authors. CMEs which are launched inside the solar activity belts at a time before the solar maximum and which possess a total plasma and magnetic pressure less than the ambient solar wind, are often deflected to the latitude where the slow solar wind resides.

After deriving the 3D localization of the CME cloud, we also localize the part of the CME leading edge around the solar equatorial plane directed to Venus. In Figure 13, the corresponding height–time (HT) plot is presented in the left panel. The last point in the HT diagram is derived from *VEX* data. It corresponds to the arrival of the ICME at Venus at around 11:00 UT on August 10. The x axis is in units of hours starting from the beginning of August. On the right side of Figure 13, the speed is calculated from the HT plot with an exponential fit. The fit is constrained by HT data on the left. The *VEX* data point was included such that the respective travel time of the speed agrees with the distance to Venus. We conclude from the low asymptotic speed of about 430 km s^{-1} that the CME was embedded in the slow solar wind, which severely decelerated the CME.

5. CONCLUSIONS AND DISCUSSIONS

We have developed a new method to obtain the 3D shape of a CME cloud without assuming a predefined family of shape functions. We applied our method to a CME which erupted on 2010 August 7. The geometric center, three principal axes, and the corresponding scale along them were derived and their evolution with time is presented. We could observe the evolution

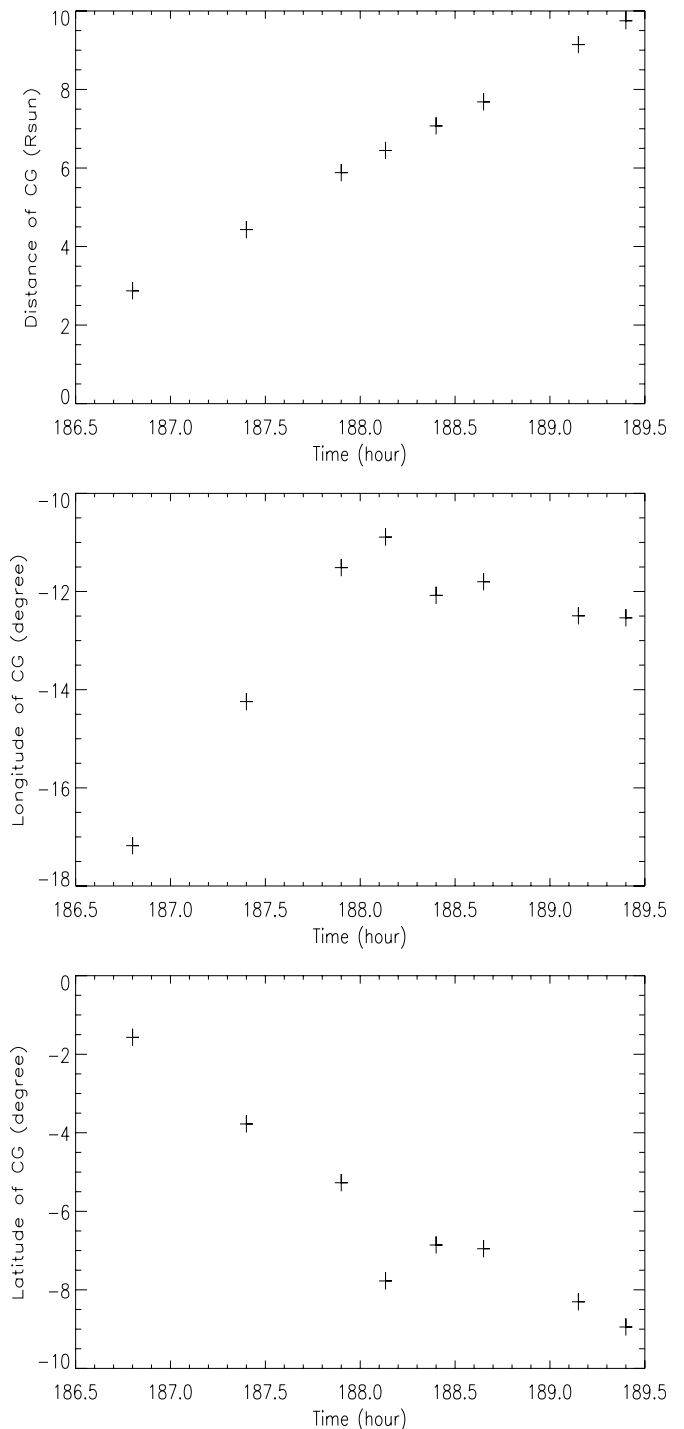


Figure 12. From top to bottom are the time evolution of the distance of GC to the Sun center, the longitude, and the latitude of GC in units of degree.

of the CME shape for approximately 3 hr. We find that a significant deformation occurred during the first two hours. During the last hour of observation, the shape evolution was more limited and continued almost self-similarly. We attribute the change of the CME morphology during the first two hours to its interaction with the ambient solar wind. The projected CME major axes are found not perpendicular to the propagation direction. It is probably due to the east–west asymmetry of the CME related filament eruption.

The determination of the CME shape is helpful in interpreting the in situ observations by *VEX/MAG*, *STEREO A* &

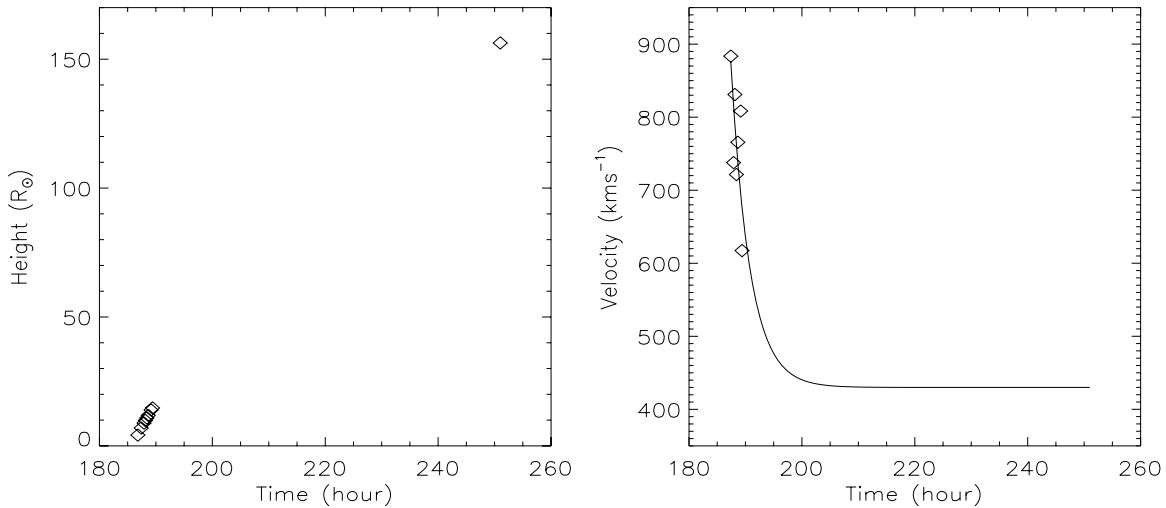


Figure 13. Left: height–time profile of the part of CME periphery heading to Venus. Right: the corresponding speed profile with an exponential function fitting to it.

B/IMPACT, *STEREO A & B/PLASTIC*, and *ACE*. *VEX* detected a magnetic cloud following the preceding shock; *STEREO B* only saw the shock. This is supported by our reconstruction which, if extrapolated out to 1 AU, predicts that the CME just missed the location of *STEREO B*. For *ACE*, the shock had probably dissolved into the background solar wind before it arrived at the Earth. Therefore, *ACE* did not detect any shock signature.

By extrapolating the CME geometric center propagation direction backward to the solar surface, we find that the source region of this CME is likely the active region AR 11093 located at N12E31 in which an M1.0 class flare occurred about 40 min before the CME became visible in the *STEREO* coronagraphs. The rise of the destabilized filament led to CME eruption. The orientation of the polarity inversion line in AR 11093 is, in general, consistent with the major principal axes of the CME shape we have obtained from its reconstructed shape. However, it is not consistent with the flux rope axis deduced from the *VEX* data with the MVA method. According to the reconstructed CME localization in the equatorial plane, it is very probable that only the leg of the CME flux rope passed the *VEX* spacecraft. Indeed, the flux rope observed showed a strong inclination in the radial direction.

A comparison of the latitude of the source region with the latitude of geometric center of the reconstructed 3D CME implies there is a southward component of its motion. If the plasma pressure and magnetic pressure in the CME is less than that of the background solar wind, the CME is often deflected away from the coronal hole where the fast solar wind dominates.

Combining the remote-sensing measurement and the in situ data from *VEX*, we derive the 3D distance and speed evolution of the CME motion from Sun to Venus. The CME speed decreases from 900 km s^{-1} at one hour after its initiation to 430 km s^{-1} . Probably the CME speed was finally adjusted to the ambient solar wind flow.

Temmer et al. (2012) investigated at which heliospheric distance the drag force starts to prevail over the driving magnetic force so that the speed of the ICME gets finally adjusted to the speed of the ambient solar wind. They analyzed the observations of different CMEs and found that this heliospheric distance varies considerably from below $30 R_{\odot}$ to beyond 1 AU. Theoretical and observational work on the driving and drag forces during the CME evolution and propagation from the Sun to the interplanetary medium can also be found in Chen (1996), Manoharan

et al. (2001), Tappin (2006), and Howard et al. (2007). For the CME we have analyzed, we estimate that this distance at which the CME speed becomes adjusted to the solar wind speed is beyond the FOV of COR2. Therefore, to derive a reliable speed profile, and to eventually make an accurate prediction of the CME transit time on Earth or other planets, the Heliospheric Imager I (HI 1) in the SECCHI instrument package has to at least be included for the investigated CME. In the near future, we will extend the mask fitting method to HI observations.

A precise prediction of the CME travel time also depends on the accuracy of the reconstruction method. Comparison of our mask fitting method and other 3D reconstruction methods, for example, GCS forward modeling, polarization ratio, local correlation track combined with tie-pointing, geometrical localization, etc., will be presented in another paper. For this particular CME associated with a complicated polarity inversion line, the forward modeling of the CME by a single flux rope model will probably be not very successful owing to the odd shape of the CME. A fit with two flux ropes might give better results. A shortcoming of our mask fitting method is that the internal structure of the CME is not included. We are planning to extend our shape reconstruction method by a tomographic approach to determine a constrained density distribution model within the 3D CME cloud.

We thank CDAweb for making the *STEREO/IMPACT*, *STEREO/PLASTIC* data available. Thanks to Marilena Mierla for many discussions on this work during her visit to the Max-Planck-Institut for Solar System Research. *STEREO* is a project of NASA. The SECCHI data used here were produced by an international consortium of the Naval Research Laboratory (USA), Lockheed Martin Solar and Astrophysics Lab (USA), NASA Goddard Space Flight Center (USA), Rutherford Appleton Laboratory (UK), University of Birmingham (UK), Max-Planck-Institut for Solar System Research (Germany), Centre Spatial de Liège (Belgium), Institut d’Optique Théorique et Appliquée (France), Institut d’Astrophysique Spatiale (France). L.F. and W.Q.G. are supported by grants 10833607, 11003047, and 11078025 from NSFC and 2011CB811402 from MSTC. The contribution of B.I. benefited from support of the German Space Agency DLR and the German ministry of economy and technology under contract 50 OC 0904.

REFERENCES

- Antunes, A., Thernisien, A., & Yahlil, A. 2009, *Sol. Phys.*, **259**, 199
- Brueckner, G. E., Howard, R. A., Koomen, M. J., et al. 1995, *Sol. Phys.*, **162**, 357
- Byrne, J. P., Maloney, S. A., McAteer, R. T. J., Refojo, J. M., & Gallagher, P. T. 2010, *Nature Commun.*, **1**, 74
- Chen, J. 1996, *J. Geophys. Res.*, **101**, 27499
- Cremades, H., & Bothmer, V. 2004, *A&A*, **422**, 307
- de Koning, C. A., & Pizzo, V. J. 2011, *Space Weather*, **9**, 3001
- de Koning, C. A., Pizzo, V. J., & Biesecker, D. A. 2009, *Sol. Phys.*, **256**, 167
- Domingo, V., Fleck, B., & Poland, A. I. 1995, *Sol. Phys.*, **162**, 1
- Feng, L., Inhester, B., Solanki, S. K., et al. 2007, *ApJ*, **671**, L205
- Feng, L., Inhester, B., Solanki, S. K., et al. 2009, *ApJ*, **700**, 292
- Feng, L., Wiegmann, T., Inhester, B., et al. 2007, *Sol. Phys.*, **241**, 235
- Gonzalez, W. D., Joselyn, J. A., Kamide, Y., et al. 1994, *J. Geophys. Res.*, **99**, 5771
- Gopalswamy, N., Nitta, N., Akiyama, S., Mäkelä, P., & Yashiro, S. 2012, *ApJ*, **744**, 72
- Gopalswamy, N., & Yashiro, S. 2011, *ApJ*, **736**, L17
- Howard, T. A., Fry, C. D., Johnston, J. C., & Webb, D. F. 2007, *ApJ*, **667**, 610
- Howard, R. A., Moses, J. D., Vourlidas, A., et al. 2008, *Space Sci. Rev.*, **136**, 67
- Inhester, B. 2006, arXiv:astro-ph/0612649
- Kaiser, M. L., Kucera, T. A., Davila, J. M., et al. 2008, *Space Sci. Rev.*, **136**, 5
- Lemen, J. R., Title, A. M., Akin, D. J., et al. 2012, *Sol. Phys.*, **275**, 17
- Liewer, P. C., de Jong, E. M., Hall, J. R., et al. 2009, *Sol. Phys.*, **256**, 57
- Liewer, P. C., Hall, J. R., Howard, R. A., et al. 2011, *J. Atmos. Sol.-Terr. Phys.*, **73**, 1173
- Liu, Y., Davies, J. A., Luhmann, J. G., et al. 2010, *ApJ*, **710**, L82
- Liu, Y., Thernisien, A., Luhmann, J. G., et al. 2010, *ApJ*, **722**, 1762
- Lugaz, N., Vourlidas, A., Roussev, I. I., & Morgan, H. 2009, *Sol. Phys.*, **256**, 269
- Manoharan, P. K., Tokumaru, M., Pick, M., et al. 2001, *ApJ*, **559**, 1180
- Mierla, M., Inhester, B., Antunes, A., et al. 2010, *Ann. Geophys.*, **28**, 203
- Möstl, C., Farrugia, C. J., Temmer, M., et al. 2009, *ApJ*, **705**, L180
- Ontiveros, V., & Vourlidas, A. 2009, *ApJ*, **693**, 267
- Reddy, V., Ajar Maurya, R., & Ambastha, A. 2012, *Sol. Phys.*, **277**, 337
- Rodriguez, L., Mierla, M., Zhukov, A. N., West, M., & Kilpua, E. 2011, *Sol. Phys.*, **270**, 561
- Rouillard, A. P., Davies, J. A., Forsyth, R. J., et al. 2009, *J. Geophys. Res. (Space Phys.)*, **114**, 7106
- Scherrer, P. H., Schou, J., Bush, R. I., et al. 2012, *Sol. Phys.*, **275**, 207
- Srivastava, A. K., & Murawski, K. 2012, *ApJ*, **744**, 173
- Tappin, S. J. 2006, *Sol. Phys.*, **233**, 233
- Tappin, S. J., & Howard, T. A. 2009, *Space Sci. Rev.*, **147**, 55
- Temmer, M., Rollett, T., Möstl, C., et al. 2012, *ApJ*, **749**, 57
- Thernisien, A. 2011, *ApJS*, **194**, 33
- Thernisien, A., Vourlidas, A., & Howard, R. A. 2009, *Sol. Phys.*, **256**, 111
- Thernisien, A. F. R., Howard, R. A., & Vourlidas, A. 2006, *ApJ*, **652**, 763
- Veronig, A. M., Muhr, N., Kienreich, I. W., Temmer, M., & Vršnak, B. 2010, *ApJ*, **716**, L57
- Wuelser, J.-P., Lemen, J. R., Tarbell, T. D., et al. 2004, *Proc. SPIE*, **5171**, 111
- Yurchyshyn, V. 2008, *ApJ*, **675**, L49
- Yurchyshyn, V. B., Wang, H., Goode, P. R., & Deng, Y. 2001, *ApJ*, **563**, 381
- Zhang, T. L., Baumjohann, W., Delva, M., et al. 2006, *Planet. Space Sci.*, **54**, 1336